Ionics (2021) 27:2159–2167
https://doi.org/10.1007/s11581-021-03987-1

ORIGINAL PAPER

Incorporation of MnO_2 nanoparticles into MOF-5 for efficient oxygen evolution reaction

Muhammad Fiaz[1,2] · Muhammad Kashif[1] · Jafar Hussain Shah[1] · Muhammad Naeem Ashiq[1] · D. H. Gregory[2] · Syeda Rabia Batool[3] · Muhammad Athar[1]

Received: 22 January 2021 / Revised: 22 February 2021 / Accepted: 24 February 2021 / Published online: 15 March 2021

Abstract

A composite MnO_2@MOF-5 is prepared by in situ incorporation of pre-synthesized MnO_2 nanoparticles into metal organic framework, MOF-5, during synthesis. The product is characterized by powder X-ray diffraction analysis, Raman spectroscopy, Fourier transform infrared spectroscopy, ultraviolet-visible spectroscopy, scanning electron microscopy, energy-dispersive X-ray spectroscopy, and elemental mapping, which support the formation of proposed composite materials. The oxygen evolution reaction activity of MnO_2@MOF-5 composite is evaluated by cyclic voltammetry, linear sweep voltammetry, and chronoamperometric measurement under visible light. It is found that MnO_2@MOF-5/NF has better durability and ability to produce a current density of 10 $mAcm^{-2}$ at only 324 mV overpotential with lower 71 $mVdec^{-1}$ Tafel slope as compared to some of previously reported Mn-based catalysts for oxygen evolution reaction (OER). The stability of these electrodes is evaluated by chronoamperometric studies for 6000 s in the presence of visible light, and they showed constant current density. Furthermore, the stability studied by continuous CV sweeps in 1.0 M NaOH at a scan rate of 100 mVs^{-1} shows that these materials are stable up to 100 cycles, which confirms the stability and durability of the electrodes.

Keywords MOF-5 · MnO_2 nanoparticles · In situ incorporation · Linear sweep voltammetry · Oxygen evolution reaction

Introduction

Increasing environmental pollution and the rapid decrease of fossil fuels have diverted the attention of researchers towards the development of new alternate sources of energy [1]. Over the past few decades, many efforts have been made in this regard, and it has been found that hydrogen can be used as a clean, secure, non-polluting, and environment friendly source of energy [2]. Hydrogen can be produced from the hydrogen-containing compounds like fossil fuels and biomass, but they contaminate the environment [3]. Alternately, hydrogen can be effectively produced by photocatalytic water splitting which has no harmful effect upon the environment [4]. The production of hydrogen by water splitting has attracted great attention after first reported by Fujishima and Honda in 1972 [5].

During water splitting, hydrogen and oxygen are produced at the surface of catalyst due to redox reaction [6]. Currently, Ru/Ir-based OER-based catalysts have emerged as the best OER catalysts, but due to their low earth abundant and high cost, they cannot be used at commercial levels [7, 8]. So, the development of highly active OER catalyst based on low-cost earth abundant 3D-element has attracted a huge research attention. Therefore, up until now, more than a hundred different materials have been reported as catalyst for water splitting [9]. However, high electron-hole pair recombination lowers the solar energy conversion and reduces the efficiency of catalysts [10]. Many efforts have been made to solve this problem, but efficiency has not been increased up to satisfactory level [11].

In the recent years, metal organic frameworks (MOFs) have emerged as potential candidate for different applications such as storage [12], separation [13], catalysis [14], and biological imaging [15]. MOFs have unique properties such as high surface area and large number of cavities and channels [16]. In 2010, Garcia and co-workers reported Zr-containing MOFs known as

✉ Muhammad Athar
athar.qr@gmail.com

[1] Institute of Chemical Sciences, Bahauddin Zakariya University, Multan 60800, Pakistan

[2] WestCHEM School of Chemistry, University of Glasgow, G12 8QQ, Glasgow, UK

[3] Institute for Chemical and Bioengineering, ETH Zurich, 8093 Zurich, Switzerland

UiO-66 and UiO-66 (NH_2) as prominent catalysts for water splitting in the presence of visible light [17]. It has been observed that both UiO-66 and UiO-66 (NH_2) have greater catalytic activity towards water splitting when Pt nanoparticles are incorporated within the pores [18]. Since then, many successful efforts have been made for the preparation of composites of MOFs by incorporation of different materials such as metal/metal oxide nanoparticles [19], quantum dots [20], graphene [21], dense and porous silica nanospheres [22], and magnetic beads [23] to get specific properties. In MOFs, the organic ligands serve as antenna to harvest light and activate the metal. Photogenerated electrons produced in MOFs are transferred to nanoparticles and increase the charge separation for efficient photocatalytic activity [24].

Manganese-based oxides (MnO_x) nanomaterials have been emerged as efficient OER catalysts due to their unique properties such as well-controlled morphology and electronic state [25, 26]. Manganese oxide (MnO_2) nanoparticles, due to their stability, large surface area, and small size [27], are used in redox reactions [28] and catalysis [29]. MOF-5 is an important metal organic framework that consists of $[Zn_4O]^{6+}$ clusters linked by octahedral arrangement of 1,4-benzenedicarboxylate groups to form a cubic porous framework of MOF-5 [30]. In the present work, nanoparticles of MnO_2 have incorporated into MOF-5 to form MnO_2@MOF-5 composite. Different experimental conditions are tested, and composite materials showed superior OER performance to individual MnO_2 particles.

Experimental

Chemicals

The chemicals used for the synthesis of materials were zinc acetate dihydrate, $Zn(CH_3COO)_2.2H_2O$, 1,4-benzenedicarboxylic acid (H_2BDC), triethylamine (TEA), *N*,*N*-dimethylformamide (DMF), $KMnO_4$, $MnSO_4.H_2O$, and H_2O_2. All these chemicals were purchased from Merck. These were of analytical grade and used as such without any further purification.

Synthesis of MnO_2@MOF-5 composite

Hydrothermal method was used for the preparation of nanoparticles of MnO_2 as reported in literature [31]. MnO_2@MOF-5 composite was prepared by incorporation of pre-synthesized nanoparticles of MnO_2 into MOF-5 during its synthesis. In a typical procedure, a suspension of 10 mg MnO_2 nanoparticles was prepared in 20 mL DMF. The suspension was added into 100 mL DMF solution containing 2.7 g $Zn(CH_3COO)_2.2H_2O$. Then a 50 mL DMF solution containing 0.8 g H_2BDC and 2 mL TEA was added dropwise to the mixture under constant magnetic stirring. The whole mixture was stirred at room temperature for 24 h. The brownish precipitates were obtained and collected by centrifugation, washed with distilled water and DMF several times. The resulting product was dried at 50 °C in a vacuum oven for 3 h and activated at 120 °C for 6 h. The dried precipitates were ground and stored for further characterization and photoelectrochemical studies. A sample of pure MOF-5 was also prepared by the same procedure without adding MnO_2 nanoparticles.

Oxygen evolution reaction studies

The oxygen evolution reaction studies of synthesized samples were studied in the presence of visible light as well as in the dark at room temperature by cyclic voltammetry (CV), linear sweep voltammetry (LSV), and chronoamperometry using the electrochemical workstation (Autolab PG station 204) in 1.0 M NaOH aqueous electrolyte at various scan rates. The electrochemical measurements were conducted using a three-electrode setup containing Ag/AgCl as reference electrode and Pt-wire as counter electrode. All the applied potentials were converted into reversible hydrogen electrode (RHE) by using following equation

$$E_{RHE} = E_{Ag/AgCl/Sat.KCl} + 0.059\ pH + 0.197 \quad (1)$$

LSV was measured at 1 mVs^{-1} scan rate, and it was used to evaluate Tafel plot according to following equation:

$$\eta = a + b \log j \quad (2)$$

where η is the overpotential, j is the current density, and b is the Tafel slope. For OER, the overpotential was calculated by the following equation:

$$\eta = E_{RHE} - 1.23 \quad (3)$$

The working electrode was prepared on a nickel foam (NF). For the preparation of working electrode, a piece of NF (1 cm × 1 cm) was cleaned with ethanol and acetone by sonication for 30 min, respectively, washed with distilled water, and dried at room temperature. In total, 10 mg of the prepared sample was added in distilled water to make the slurry, which was then uniformly pasted on the NF and dried at 50 °C for overnight. CV, LSV, and chronoamperometric measurements used the dried NF containing sample as working electrode for the study of water splitting activity. It was observed from SEM images that the catalytic material remains deposited on the surface of Ni foam before and after photoelectrochemical reaction (Fig. 1). It indicated the significant stability of these working electrodes for PEC studies.

Characterization

Powder X-ray diffraction (XRD) patterns of pure MOF-5 and MnO_2@MOF-5 were recorded on a Shimadzu XRD

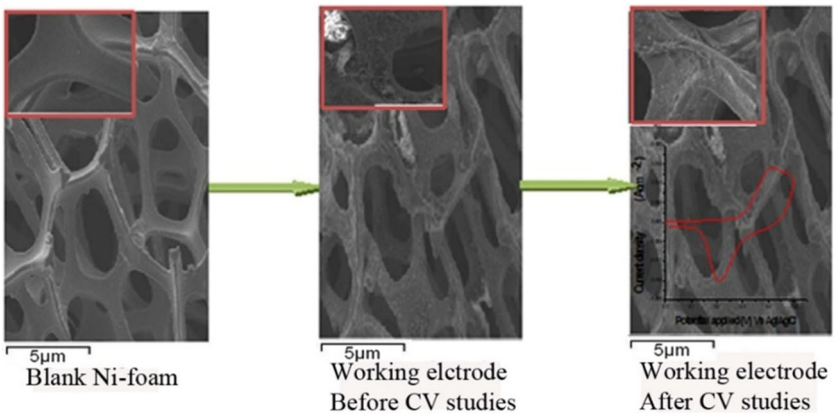

Fig. 1 Schematic representation of coating on the Ni foam and its use for photoelectrochemical study; inset are the magnified images of blank Ni foam and working electrode before CV studies and after CV studies

diffractometer with Cu-Kα radiation (λ = 0.15406 nm) in the range of 2θ between 10° and 80° at scan rate of 5° min^{-1}. Raman spectrometry was carried out by using the Horiba Jobin-Yvon Lab RAM HR800 Raman spectrometer in the range from 100 to 2000 cm^{-1}. The 532-nm solid-state laser was used to avoid florescence and decomposition of samples. The output power was reduced to 10%, and the acquisition time ranged from 5 to 10 min. Fourier transform infrared spectra were obtained by using Nicolet Nexus 870 in range from 4000 to 400 cm^{-1}.The morphology and composition of samples were studied by scanning electron microscopy (SEM) by using the Philips XL30 Environmental SEM attached with Oxford Instrument Inca 500 energy-dispersive X-ray (EDX) spectrometer. The optical properties of the samples were studied by using the Shimadzu UV-2600 UV-visible spectrophotometer at room temperature in the range between 200 and 900 nm.

Results and discussion

Powder XRD patterns of MOF-5 and MnO_2@MOF-5 are shown in Fig. 2; both the materials have grown well in crystalline form and intense peaks are observed. The P-XRD pattern of pure MOF-5 matches well with that reported in literature [32, 33]. In the P-XRD pattern of MnO_2@MOF-5, the peaks that index to both MnO_2 and MOF-5 are observed, and well-defined diffraction peaks at 2θ about 19.18°, 20.47°, and 30.52° correspond to MOF-5 and 13.55°, 18.61°, 28.45°, 38.65°, 41.11°, and 50.13° to MnO_2. The diffraction peaks correspond to MnO_2 matches with the standard XRD pattern ICSD 44-141. From the P-XRD patterns of MOF-5 and MnO_2@MOF-5, it is observed that the host MOF-5 maintains its characteristic reflection pattern and crystallinity.

The Raman spectra of MOF-5 and MnO_2@MOF-5 are shown in Fig. S1 (Supplementary information). The Raman spectrum of MOF-5 consists of five strong Raman bands at 635 cm^{-1}, 865 cm^{-1}, 1139 cm^{-1}, 1448 cm^{-1}, and 1615 cm^{-1}, and these are in accordance with the results reported in literature [34]. These Raman bands are due to vibrational modes of benzene rings and vibration modes of carboxylate groups [35]. Similarly, the Raman spectrum of MnO_2@MOF-5 also consist of five Raman bands at 635 cm^{-1}, 865 cm^{-1}, 1141 cm^{-1}, 1434 cm^{-1}, and 1615 cm^{-1}, which indicates that MOF-5 shows its dominance and maintains its crystalline structure. In the Raman spectrum of MnO_2@MOF-5, slight Raman shifts can be observed at 1141 cm^{-1} and 1434 cm^{-1} which may be due to the interaction of MnO_2 with $[Zn_4O]^{6+}$ clusters of MOF-5 and some displacement of organic ligand.

These five vibrational modes of MOF-5 and MnO_2@MOF-5 are comparable with DFT quantum calculations of MOF-5 as reported previously [36]. The Raman spectra of MnO_2@MOF-5 do not contain characteristic peaks of MnO_2 because the dominance of host MOF, peaks of MnO_2, is masked.

The FTIR spectra of both MOF-5 and MnO_2@MOF-5 are shown in Fig. S2. The FTIR spectra of MOF-5 shows two sharp vibrational peaks at 1575 cm^{-1} and 1370 cm^{-1} due to symmetric and asymmetric stretching vibration of C-O, whereas MnO_2@MOF-5 shows vibrational bands at 1586 cm^{-1} and 1377 cm^{-1} due to symmetric and asymmetric stretching vibration of C-O bonded to Zn, respectively. In the FTIR spectra of MOF-5, symmetric stretching vibration of Zn_4O appears at 642 cm^{-1} [37]. A strong peak appears at 530 cm^{-1} in the FTIR spectrum of MnO_2@MOF-5 which may be due to the overlapping of Mn-O vibration with secondary building unit of MOF-5, coordinated $[Zn_4O]^{6+}$ cluster.

The morphology and composition of MOF-5 and MnO_2@MOF-5 was studied by scanning electron microscopy and SEM-based EDX, respectively. The SEM images are shown in Fig. 3, which shows that MOF-5 has grown in crystalline form having a rectangular shape (Fig. 3a–b). Figure 3d–e shows the SEM images of MnO_2@MOF-5 composite which indicates that MnO_2@MOF-5 also have morphologically smooth surface of the crystals. The EDX spectra of MOF-5 and MnO_2@MOF-5 are shown in Fig. 3c and f, respectively. Figure 3c shows that the EDX spectrum of MOF-5 contains all the three elements (Zn, C, and O) of MOF-5. Similarly, Fig. 3f shows that the EDX spectrum of

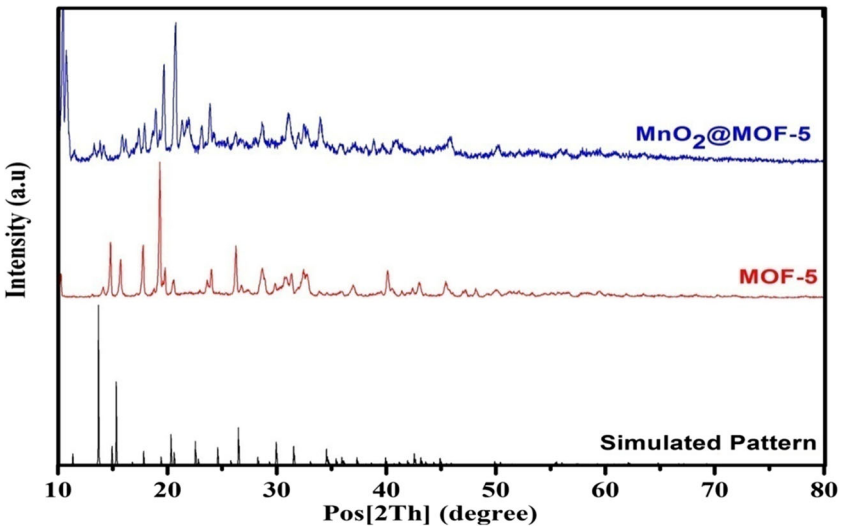

Fig. 2 Powder XRD patterns of MOF-5 and MnO_2@MOF-5 in comparison with simulated pattern of MOF-5

MnO_2@MOF-5 composite contains all the four elements (Zn, Mn, C, and O) and indicated successful incorporation of MnO_2 into MOF-5.

The elemental mapping analysis of MOF-5, as shown in Fig. 4a–d, shows that there is a uniform and homogeneous distribution of elements, and it has grown in a rectangular shape. Figure 4a–c show elemental mapping of MOF-5 for Zn, C, and O respectively and Fig. 4d is the mix mapping of the metal organic framework, MOF-5, which indicated that all the basic elements are uniformly and homogenously distributed in the sample. Similarly, Fig. 4e–g show the elemental mapping of MnO_2@MOF-5 for Mn, Zn, and O respectively and Fig. 4h is the mix mapping of MnO_2@MOF-5, which indicated that nanoparticles of MnO_2 has been successfully incorporated within MOF-5 as it can be observed that Mn is uniformly distributed in the composite.

The optical properties of synthesized samples were studied by UV-visible absorption spectrophotometry. As shown in Fig. S3, MOF-5 has maximum absorption in UV-region at 265 nm due to $\pi \rightarrow \pi^*$ electronic transition of 1,4-BDC linkers and with no significant absorption in visible light. After incorporation of MnO_2 into MOF-5, its λ_{max} shifts from 265 to 275 nm. Furthermore, a new absorption peak having λ_{max} around 400 nm has introduced with increase in absorption in the visible region. Such a modification increases the charge separation because photogenerated electron efficiently transfer from organic ligand 1,4-BDC to $[Zn_4O]^{6+}$ clusters of MOF-5 and then to MnO_2, similar to UIO-66(NH_2) and Ti-MOF-NH_2.

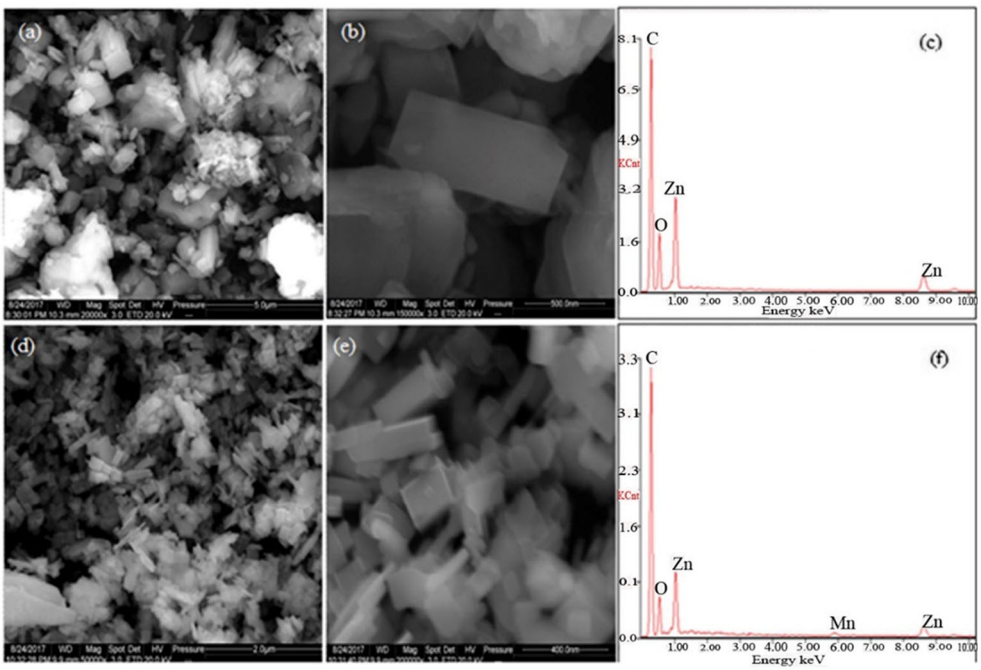

Fig. 3 (**a**–**b**) SEM images, (**c**) EDX of MOF-5, and (**d**–**e**) SEM images; (**f**) EDX of MnO_2@MOF-5

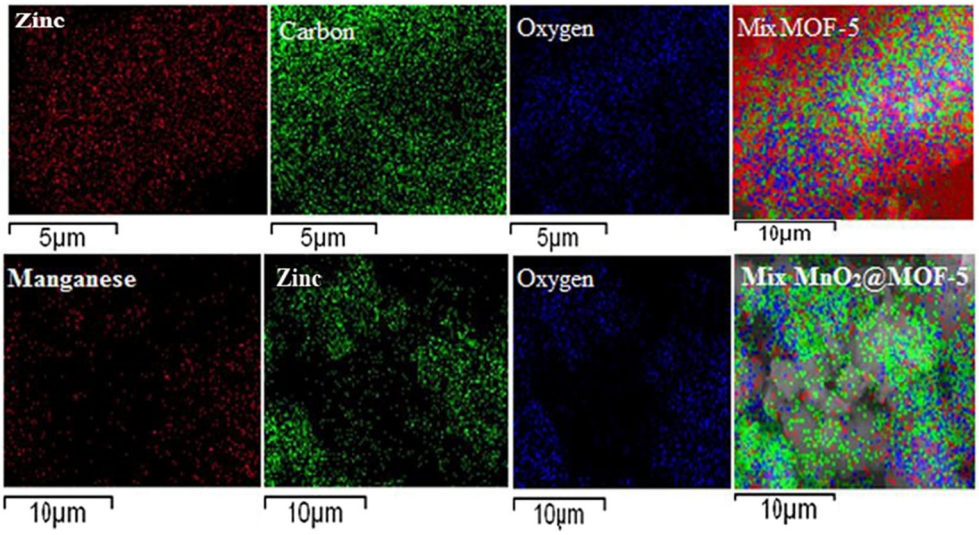

Fig. 4 Elemental mappings of MOF-5 and MnO_2@MOF-5

The increase of charge separation has improved the photoelectrochemical activity. The band gap of a semiconductor can be calculated from Tauc plot by linear extrapolation of absorption edge by using the following equation:

$$\alpha h\nu \propto \left(h\nu - E_g\right)^{0.5} \quad (4)$$

where α is the absorption coefficient, h is the Planck's constant, and ν is the wavenumber.

The band gap of MOF-5 is determined to be 3.70 eV, which is in accordance with the literature reported previously [38], while the band gap of MnO_2@MOF-5 is 2.47 eV, which indicated that the incorporation of MnO_2 nanoparticles brings the band gap of MOF-5 into the visible region. Hence, it increases the absorption of visible light and improves the photoelectrochemical activity of MnO_2@MOF-5. The mechanism of increase of charge separations is proposed in a schematic representation as shown in Fig. 5.

Photoelectrochemical OER analysis

Firstly, photoelectrochemical studies towards OER are determined by cyclic voltammetry. CV curves of these electrodes are recorded using 1.0 M NaOH electrolyte both in the presence of dark and under visible light at different scan rates (10, 20, 30, 40, 50, and 100mVs^{-1}) for MOF-5/NF and (5, 10, 20, 30, 40, 50, 60, 70, 80, 90, and 100mVs^{-1}) for MnO_2/NF and MnO_2@MOF-5/NF. It is found that all the working electrodes delivered almost zero current density in the dark due to the absence of OER activity. Figure 6a shows that MOF-5/NF generates no significant current density at various scan rates within RHE potential range of 0.2 to 1.2 V. Figure 6b and c showed CV curves for MnO_2/NF and MnO_2@MOF-5/NF electrodes under RHE potential range 1.0 to 1.6 V, in the dark as well as in visible light. It is investigated from the CV curves of MnO_2/NF and MnO_2@MOF-5/NF that in the presence of visible light, a prominent increase in current density is observed, due to OER activity. However, pre-OER oxidation-reduction peaks appeared in the CV curves of MnO_2/NF and MnO_2@MOF-5/NF due to redox reaction of Ni(II)/Ni(III) [39]. In MnO_2/NF, the oxidation and reduction peaks appeared in the range between 1.44 and 1.50 V and 1.38 and 1.34 V, respectively. The CV curves of MnO_2@MOF-5/NF electrode showed that there are two oxidation peaks at various scan rates (10 to 100mVs^{-1}), first between 1.35 and 1.41V and then between 1.40 and 1.47 V, and only one reduction peak is observed between 1.28 and 1.20 V. It is revealed from the comparison of CV curves of MOF-5/NF, MnO_2/NF, and MnO_2@MOF-5/NF that MnO_2@MOF-5/NF has higher current density as compared to pure MOF-5/NF and MnO_2/NF due to the hetero-junction formation between MnO_2/NF and the central metallic cluster of MOF-5. Thus, synergistic effect and hetero-junction formation played a significant role to enhance the OER activity of MnO_2@MOF-5/NF as compared to all other synthesized samples. The inset of Fig. 6b and c represented the anodic and cathodic peak current density with respect to the scan rate of MnO_2/NF and MnO_2@MOF-5/NF, respectively.

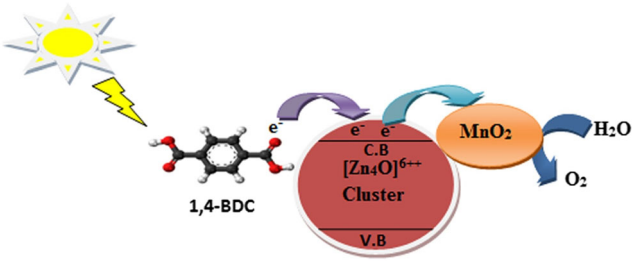

Fig. 5 Schematic representation of increased charge separation and water splitting by MnO_2@MOF-5

The catalytic activities of MOF-5/NF, MnO_2/NF, and MnO_2@MOF-5/NF electrodes are further evaluated by linear sweep voltammetry (LSV) in the presence of visible light in 1 M NaOH electrolyte, as shown in Fig. 7a. As in CV, the anodic

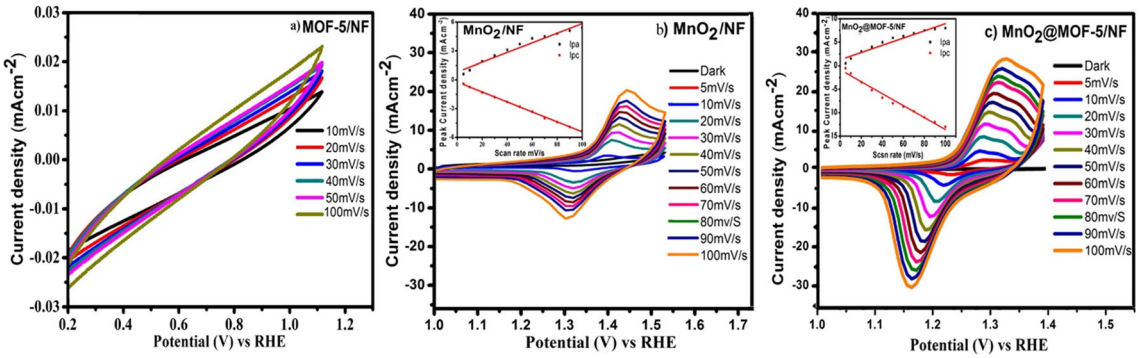

Fig. 6 CV curves of MOF-5/NF (**a**) and MnO_2/NF (**b**); inset is peak current density vs scan rate and MnO_2@MOF-5/NF (**c**). Inset is peak current density vs scan rate at different scan rates

oxidative peak is observed in LSV of both MnO_2/NF and MnO_2@MOF-5/NF due to oxidation of $Ni^{2+} \rightarrow Ni^{3+}$ from the Ni foam. The LSV curve of MOF-5/NF electrode indicated that there is no significant generation of current density; even at very high overpotential, it generated just 0.46 $mAcm^{-2}$ current density. For a comparison between MnO_2/NF and MnO_2@MOF-5/NF, the overpotential required to achieve 2 $mAcm^{-2}$current density is considered. It is observed that MnO_2@MOF-5/NF required a low overpotential of 284 mV to achieve 2 $mAcm^{-2}$ current density, whereas MnO_2/NF required 324 mV overpotential for 2 $mAcm^{-2}$. It is observed that MnO_2@MOF-5/NF delivered the benchmark of 10 $mAcm^{-2}$ at an overpotential of 324 mV, which could be comparable and even less than some of reported Mn-based and other 3d transition metal–based catalyst for OER, represented in Table 1. Furthermore, to understand the kinetics of MnO_2@MOF-5/NF towards OER, a Tafel plot is derived from LSV. The calculated Tafel slope value for MnO_2@MOF-5/NF is just 71 $mVdec^{-1}$, which is lower than MnO_2/NF (157 $mVdec^{-1}$) and previously reported Mn-based materials such as MnO_2/Ni-Co carbonate precursor/NF (95

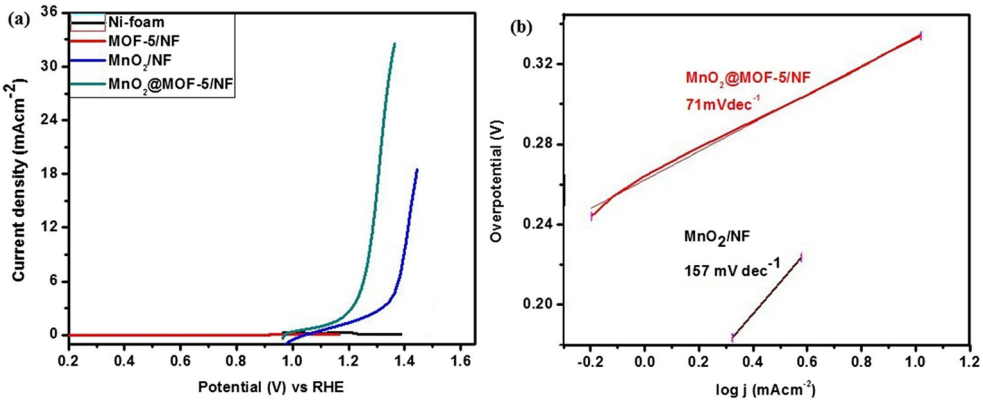

Fig. 7 **a** LSV curves of MOF-5/NF, MnO_2/NF, and MnO_2@MOF-5/NF. **b** Tafel plot for MnO_2/NF and MnO_2@MOF-5/NF

Table 1 The comparison of OER activity of MnO_2@MOF-5/NF with previously reported Mn-based and other 3D transition metal–based OER catalyst

Catalyst	Overpotential (mV) for 10 $mAcm^{-2}$ current density	Reference
Co^{2+}/MnO_2	360	ACS Catal. 2016, 6, 7739.
Ni^{2+}/MnO_2	400	Angew Chem. Int. Ed. 2016, 55, 10381
α-MnO_2	490	J. Am.Chm. Soc. 2014, 136, 11452.
Metal-ion doped MnO_2	390	Adv. Funct. Mater. 2017, 27, 1704083
CoMnP	330	J. Am.Chm. Soc. 2016, 138, 4006.
AuNi heterodimers	350	Small 2018, 14, 1703749
Co_9S_8@NOSC-900	330	Adv. Funct. Mater. 2016, 26, 4712.
Fe-doped mesoporous Co_3O_4	380	Chem. Commun. 2014, 50, 10122.
α-MnO_2/$CDs_{0.25}$	352	Electrochim. Acta 2020, 337, 135823
MnO_2@MOF-5/NF	324	This work.

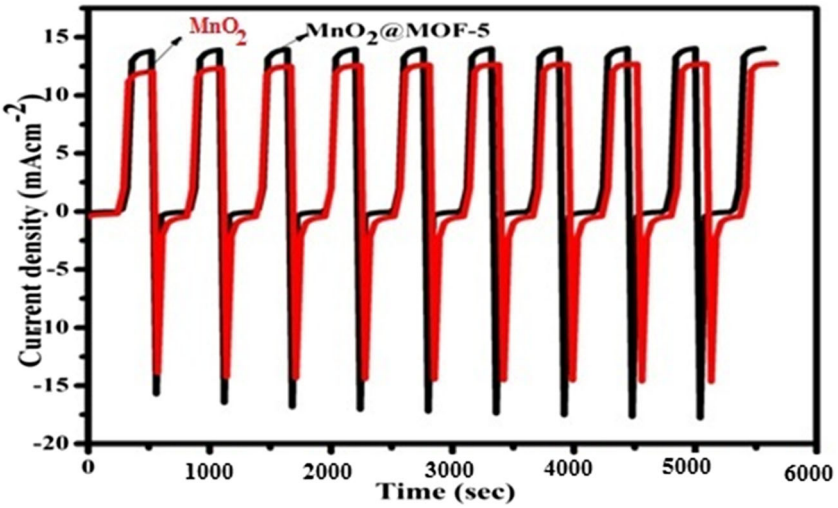

Fig. 8 Chronoamperometric measurements of MnO_2/NF and MnO_2@MOF-5/NF at 1.0 V applied potential

$mVdec^{-1}$) and $MnO_2/NiCo_2O_4$/NF (139 $mVdec^{-1}$) [40]. The lower Tafel slope value for MnO_2@MOF-5/NF indicated that it has more favorable electron transferred and improved catalytic activity as compared to MnO_2/NF, and its rate-determining step for OER was the first electron transferred as shown below,

$$M + OH^- \rightarrow MOH + e^- \quad (5)$$

where M is the catalytic active site [37, 38].

From the comparison of LSV curves, it can be found that as a result of the incorporation of MnO_2 into MOF-5 and due to synergistic effect, MnO_2@MOF-5/NF has improved OER catalytic activity over both pure MOF-5/NF and MnO_2/NF.

The stability of the synthesized materials during OER activity is evaluated by chronoamperometric studies (Fig. 8). It is observed that MnO_2@MOF-5/NF generated constant current density at constant applied voltage of 1.0 V for 6000 s in the presence of visible light. The stability of MnO_2/NF was also constant during this time, but it produced less current density.

Furthermore, the stability of MnO_2/NF and MnO_2@MOF-5/NF is studied by continuous CV sweeps in 1.0 M NaOH at a scan rate of 100 mV/s for 100 cycles. The CV curves revealed negligible degradation after 100 cycles of CV scanning, which confirmed the stability and durability of these electrodes. Figure S4 (a and b) represented the 1st and 100th cycles of CV curves at 100 mV/s of these electrodes, and it revealed almost the same curves with negligible difference.

Conclusions

MnO_2@MOF-5 composite has been synthesized successfully by in situ incorporation of pre-synthesized MnO_2 nanoparticles into MOF-5 and used as efficient OER catalyst. The MnO_2@MOF-5 composite has shown better OER activity as compared to MnO_2 and MOF-5. MnO_2@MOF-5 can expose active sites more effectively due to the incorporation of MnO_2 nanoparticles and synergistic effect. The incorporation of MnO_2 nanoparticles leads a strong electron interaction among 1,4-BDC (1,4-benzenedicarbxylate), $[Zn_4O]^{6+}$ clusters, and MnO_2 and further optimizes the charge transfer; so charge separation increased and electron-hole pair recombination decreased. Furthermore, binder's free formation of MnO_2@MOF-5/NF enhanced the electrical conductivity. The CV, LSV, and chronoamperometric results show that MnO_2@MOF-5 is an efficient OER catalyst and has more stability. This study will encourage for designing more versatile efficient materials by nanoparticle incorporation into MOFs for water splitting, fuel cells, supercapacitors, and batteries.

Supplementary Information The online version contains supplementary material available at https://doi.org/10.1007/s11581-021-03987-1.

Acknowledgements Authors acknowledge Higher Education Commission (HEC) of Pakistan for financial support, Prof. Duncan H. Gregory from School of Chemistry, University of Glasgow, UK for providing lab facilities for this work under IRSIP and Dr. Muhammad Mazhar, Distinguished National Professor, Fatima Jinnah Women University, Rawalpindi and National University of Science, Islamabad for his valuable suggestions.

Declarations

Conflict of interest The authors declare no competing interests.

References

1. Alfaifi B, Ullah H, Alfaifi S, Tahir A, Mallick T (2018) Photoelectrochemical solar water splitting: from basic principles to advanced devices. Veruscript Functional Nanomaterials ; 2

2. Stolarczyk JK, Bhattacharyya S, Polavarapu L, Feldmann J (2018) Challenges and prospects in solar water splitting and CO_2 reduction with inorganic and hybrid nanostructures. ACS Catal 8:3602–3635
3. Li R (2017) Latest progress in hydrogen production from solar water splitting via photocatalysis, photoelectrochemical and photovoltaic-photoelectrochemical solutions. Chin J Catal 38:5–12
4. Yilmaz F, Balta TM, Selbas R (2016) A review of solar based hydrogen production methods. Renew Sust Energ Rev 56:171–178
5. Fujishima A, Honda K (1972) Electrochemical photolysis of water at a semiconductor electrode. Nature 238:37–38
6. Maeda K, Damen K (2010) Photocatalytic water splitting: recent progress and future challenges. J Phys Chem Lett 1:2655–2661
7. Suen NT, Hung SF, Quan Q, Zhang N, Xu YJ, Chen HM (2017) Electrocatalysts for the oxygen evolution reaction: recent development and future perspectives. Chem Soc Rev 46:337–365
8. Strasser P (2016) Free electrons to molecular bonds and back: closing the energetic oxygen reduction (ORR) oxygen evolution reaction (OER) cycle using core-shell nanoelectrocatalysts. Acc Chem Res 49:2658–2668
9. Longhzhu L, Changhai L, Yangyang Q, Naotoshi M, Zhidong C (2017) Convex-nanorods of a-Fe_2O_3/CQDs heterojunction photoanode synthesized by a facile hydrothermal method for highly efficient water oxidation. Int J Hydrog Energy 42:19654–19663
10. Junqi L, Jian Z, Hongjuan H, Weijia L (2017) Controlled synthesis of Fe_2O_3 modified Ag-$_{010}BiVO_4$ heterostructures with enhanced photoelectrochemical activity toward the dye degradation. Appl Surf Sci 399:1–9
11. Guanying D, Bin D, Lei L, Weiwei Z, Yujie L, Honglong S (2017) Synthesis and their enhanced photoelectrochemical performance of ZnO nanoparticles-loaded CuO dandelion heterostructures under solar light. Appl Surf Sci 399:86–94
12. Kapelewski MT, Runcevski T, Tarver JD, Jiang HZH, Hurst KE, Parilla PA, Ayala A, Gennett T, FitzGeraled SA, Brown CM, Long JR (2018) Record high hydrogen storage capacity in the metal organic framework Ni_2(m-dobdc) at near-ambient temperatures. Chem Mater 30:8179–8189
13. Mansour O, Kawas G, Rasheed MA, Sakur AA (2018) Applications of metal organic framework (MOFs) to separation analytical techniques. Research J. Pharm Technol 11:3514–3522
14. Wee LH, Bonino F, Lamberti C, Bordiga S, Martens JA (2014) Cr-MIL-101 encapsulated Keggin phosphotungstic acid as active nanomaterial for catalyzing the alcoholysis of styrene oxide. Green Chem 16:1351–1357
15. Corma A, Garcia H, iXamena FXL (2010) Engineering metal organic framework for heterogeneous catalysis. Chem Rev 110: 4606–4655
16. Kreno LE, Leong K, Farha OK, Allendorf M, Van RP D, Hupp JT (2012) Metal organic framework materials as chemical sensors. Chem Rev 112:1105–1125
17. Gomes SC, Luz I, iXamena FXL, Corma A, Garcia H (2010) Water stable Zr-benzenedicarboxylate metal organic framework as photocatalyst for hydrogen generation. Chemistry 16:11133–11138
18. Peng R, Wu CM, Baltrusaitis J, Dimitrijevic NM, Rajh T, Koodali RT (2013) Ultra-stable CdS incorporated Ti-MCM-48 mesoprous materials for efficient photocatalytic decomposition of water under visible light illumination. ChemCommun 49:3221–3223
19. Sugikawa K, Nagata S, Furukawa Y, Kokado K, Sada K (2013) Stable and functional gold nanorod composites with a metal organic framework crystalline shell. Chem Mater 25:2565–2570
20. He L, Liu Y, Liu J, Xiong Y, Zheng J, Liu Y, Tang Z (2013) Core shell noble metal@metal organic framework nanoparticles with highly selective sensing property. Angew Chem Int Ed 52:3741–3745
21. Buso D, Jasieniak J, Lay MDH, Schiavuta P, Scopece P, Laird J, Amenitsch H, Hill AJ, Falcaro P (2012) Highly luminescent metal organic framework through quantum dot doping. Small 8:80–88
22. Petit C, Bandosz TJ (2009) MOF-graphite oxide composites: combining the uniqueness of graphene layers and metal-organic frameworks. Adv Mater 21:4753–4757
23. Buso D, Nairn KM, Gimona M, Hill AJ, Falcaro P (2011) Fast synthesis of MOF-5 microcrystals using sol-gel SiO_2 nanoparticles. Chem Mater 23:929–934
24. Meyer K, Ranocchiari M, Bokhoven JAV (2015) Metal organic framework for photocatalytic water splitting. Energy Environ Sci 8:1923–1937
25. Tian L, Zhai X, Wang X, Li Z (2020) Advances in manganese-based oxides for oxygen evolution reaction. J Mater Chem A 8: 14400–14414
26. Tian L, Zhai X, Wang X, Pang X, Li J, Li Z (2020) Morphology and phase transformation of α-MnO_2/MnOOH modulated by N-CDs for efficient electrocatalytic oxygen evolution reaction in alkaline medium. Electrochim Acta 337:135823–135832
27. Li Z, Cai L, Song M, Shen Y, Wang X, Li J, Wang J, Wang P, Tian L (2020) Ternary FeCoNi alloy nanoparticles in N-doped carbon nanotubes for efficient oxygen evolution reaction electrocatalysts. Electrochim Acta 339:13886–135894
28. Kim K, Daniel G, Kessler VG, Seisenbaeve GA, Pol VG (2018) Basic medium heterogeneous solution synthesis of α-MnO_2 nanoflakes as an anode or cathode in half cell configuration (vs. lithium) of Li-ion batteries. Nanomaterials 8:608–619
29. Lee HJ, Park S, Kim H (2018) Analysis of the effect of MnO_2 precipitation on the performance of vanadium/manganese redox flow battery. J Electrochem Soc 165:952–956
30. Chan ZM, Kitchaev DA, Weker JN, Schnedermann C, Lim K, Ceder G, Tumas W, Toney MF, Nacera DG (2018) Electrochemical trapping of metastable Mn^{3+} ions for activation of MnO_2 oxygen evolution catalysts. PNAS 115:E5261–E5268
31. Eddaoudi M, Kim J, Rosi N, Vodak D, Wachter J, O'Keeffe M, Yaghi OM (2002) Systematic design of pore size and functionality in isoreticular MOFs and their application in methane storage. Science 295:469–472
32. Chen Y, Duan Z, Min Y, Shao M, Zhao Y (2011) Synthesis characterization and catalytic property of manganese dioxide with different structures. J Mater Sci Mater Electron 22:1162–1166
33. Rehman A, Tirmizi SA, Badshah A, Ammad HM, Jawad M, Abbas SM, Rana UA, Khan SD (2018) Synthesis of highly stable MOF-5@MWCNTs nanocomposite with improved hydrophobic properties. Arab J Chem 11:26–33
34. Hafizovic J, Bjørgen M, Olsbye U, Dietzel PDC, Bordiga S, Prestipino C, Lamberti C, Lillerud KP (2007) The inconsistency in adsorption properties and powder XRD data of MOF-5 rationalized by framework interpenetration and the presence of organic and inorganic species in the nanocavities. J Am Chem Soc 129:3612–3620
35. Bordiga S, Lamberti C, Ricchiardi G, Regli L, Bonino F, Damin A, Lillerud KP, Bjorgen M, Zecchina A (2004) Electronic and vibrational properties of a MOF-5 metal-organic framework: ZnO quantum dot behavior. ChemCommun 20:2300–2301
36. Hu YH, Zhang L (2010) Amorphization of metal organic framework MOF-5 at unusually low applied pressure. Phys Rev B 81: 174103–174107
37. Sabouni R, Kazemian H, Rohani S (2010) A novel combined manufacturing technique for rapid production of IRMOF-1 using ultrasound and microwave energies. Chem Eng J 165:966–973
38. Yang LM, Fang GY, Ma J, Granz E, Han SS (2014) Band gap engineering of paradigm MOF-5. Cryst Gowth Des 14:2532–2541

39. Xing J, Guo K, Zou Z, Cai M, Du J, Xu C (2018) In situ growth of well-ordered NiFe-MOF-74 on Ni foam by Fe^{2+} induction as an efficient and stable electrocatalyst for water oxidation. Chem Commun 54:7046–7049
40. Yan KL, SHANG X, Gao WK, Dong B, Li X, Chi JQ, Liu YR, Chai YM, Liu CG (2017) Ternary $MnO_2/NiCo_2O_4$/NF with hierarchical structure and synergistic interaction as efficient electrocatalysts for oxygen evolution reaction. J Alloys Compd 719:314–321